J. Fluid Mech. (2015), *vol.* 768, *pp.* 375–387.
doi:10.1017/jfm.2015.106

Inviscid versus viscous instability mechanism of an air–water mixing layer

Jean-Philippe Matas†

Université Grenoble Alpes, LEGI, CNRS, F-38000 Grenoble, France

(Received 2 September 2014; revised 12 November 2014; accepted 11 February 2015; first published online 6 March 2015)

We study how confinement affects the viscous spatiotemporal instability of a two-phase mixing layer. We show that the absolute instability triggered by the inclusion of finite liquid and gas thicknesses leads to a good prediction of experimental data. In addition, this new mechanism provides a justification for the relevance of both simplified inviscid scaling laws and more sophisticated viscous approaches.

Key words: Absolute/convective instability, gas/liquid flow, shear layers

1. Introduction

The configuration in which a slow liquid stream is destabilized by a fast gas stream is both a classical fluid mechanics problem and a configuration encountered in many applications related to combustion (Lefebvre 1989). Injecting kerosene and air this way in turbo-reactors leads, for example, to the formation of a very efficient spray, i.e. one whose droplets are very small. This configuration has therefore been the object of many studies, but in spite of the attention it has garnered its mechanism is still a matter of controversy. Is it an inviscid or a viscous instability? This is the question we wish to address in the present paper.

Raynal (1997) and Raynal *et al.* (1997) carried out a series of experiments on this simple two-phase flow configuration: a slow liquid stream (velocity U_L, width 10 cm, height $H_L = 1$ cm) flowing on a solid plate is destabilized by a fast gas stream (velocity U_G, width 10 cm, height $H_G = 1$ cm). Long-wavelength waves form, and are rapidly convected away from injection and subsequently atomized into droplets. These waves have a 'long' wavelength in the sense that it is large compared to other lengths in the problem: the thicknesses of the gas and liquid streams, and especially the gas and liquid vorticity thicknesses, δ_G and δ_L. Wave frequency was measured, and experimental results confronted to a simple inviscid stability analysis generalizing that of Rayleigh (1879). Experimental trends, and a good order of magnitude of the frequency, can be captured with this approach (Raynal 1997; Raynal *et al.* 1997). The mechanism driving the instability is then similar to the classical Kelvin–Helmholtz one, but wavelength selection occurs through the size of the gas vorticity thickness δ_G. The scaling obtained for the most unstable frequency can be recovered from a simple energy budget for the velocity perturbation u, by writing that the perturbation is fed

† Email address for correspondence: matas@legi.grenoble-inp.fr

by the Reynolds stress in the gas phase:

$$\frac{\mathrm{d}\rho_L u^2}{\mathrm{d}t} = \frac{\rho_G u^2 U_G}{\delta_G} \quad \Rightarrow \quad \omega \sim \frac{\rho_G}{\rho_L}\frac{U_G}{\delta_G}, \tag{1.1}$$

where ρ_G and ρ_L are the gas and liquid densities and U_G the base flow gas velocity. This scaling law is in good agreement with experiments (Raynal 1997; Raynal *et al.* 1997). The velocity associated with these waves can be predicted by a similarly simple phenomenological argument. It is the velocity of the frame in which dynamic pressure in the liquid is balanced by dynamic pressure in the gas (Dimotakis 1986), namely,

$$U_c = \frac{\sqrt{\rho_L}U_L + \sqrt{\rho_G}U_G}{\sqrt{\rho_G} + \sqrt{\rho_L}}. \tag{1.2}$$

Measurements indicate that the experimentally measured velocity is quite close to the velocity given by (1.2) (Raynal 1997). In the limit of large gas velocities, these simple scaling laws imply in particular that the wavelength will be given by (Eggers & Villermaux 2008)

$$\lambda \sim \sqrt{\rho_L/\rho_G}\,\delta_G. \tag{1.3}$$

A similar configuration has been studied by Marmottant & Villermaux (2004), for a different geometry: a round liquid jet destabilized by an annular parallel gas stream. This study evidences the same scaling laws seen in the planar case for the frequency and wavelength of the axial wavy perturbations.

Though they capture the correct scaling laws, the values predicted by the inviscid approach underpredict wave frequency. Seeking to improve the prediction of the inviscid stability analysis, Matas, Marty & Cartellier (2011) extended it to velocity profiles mimicking the velocity deficit observed just downstream of the injection, where liquid velocity close to the interface is observed to be much smaller than in the liquid bulk. This modified analysis increases predicted frequencies by about 50 %, and therefore offers a relatively good frequency prediction. However, Matas *et al.* (2011) observed that the inviscid analysis strongly underpredicts spatial growth rates, and fails to capture the steep increase of growth rate with gas velocity.

In order to clarify the issue of the nature of the instability and of the potential effect of viscosity, Boeck & Zaleski (2005) carried out a temporal linear stability analysis including viscosity. They found that, when viscosity is included in the temporal stability analysis, the most unstable mode for the conditions of the experiments of Marmottant & Villermaux (2004) is actually a purely viscous mode. This mode is akin to the mode evidenced by Yih (1967), and discussed by Hooper & Boyd (1983, 1987) and Charru & Hinch (2000), whose mechanism in the limit of short wavelengths has been discussed by Hinch (1984): it is triggered by the jump in viscosity, and therefore in shear rate, across the interface. The order of magnitude of the growth rate associated with this viscous mode is consistent with experiments, but predicted frequencies largely overestimate experimental ones. The paradox that a simplified inviscid analysis performs better than a viscous one has been partially solved by Fuster *et al.* (2013) and Otto, Rossi & Boeck (2013): by carrying out a spatiotemporal analysis including viscosity, they showed that an absolute instability may be predicted for some of the experimental conditions of Matas *et al.* (2011), and that, when this absolute instability occurs, there is a relatively good agreement between experiments on the planar geometry and predictions. The mechanism is in this case purely viscous. However, when the instability is predicted to be convective

(for most of the experimental conditions of Matas *et al.* (2011)), frequency remains strongly overpredicted. As for growth rates, Otto *et al.* (2013) noticed that the theoretical growth rates associated with the experimentally observed frequency are in agreement with experimental ones: in other words, if another frequency selection mechanism were able to provide the experimental frequency, then frequency and growth rate would agree with experiments. Comparison with the experimental data of Marmottant & Villermaux (2004) shows a relatively good agreement, even when the instability is convective.

There are therefore two questions we want to address in this paper:

(*a*) Most of the experimental data of Matas *et al.* (2011) remain overpredicted by the spatiotemporal viscous approach of Otto *et al.* (2013), and this points to a still missing ingredient in the viscous spatiotemporal theory.

(*b*) The initial inviscid approach of Raynal (1997) and Marmottant & Villermaux (2004) seemed to capture very well experimental scaling laws. However, it is predicted by Otto *et al.* (2013) via an energy budget that the most unstable mode for the conditions of these experiments is dominated by the viscous mechanism studied by Yih (1967) and others. Why therefore is the simple inviscid approach so successful?

In the experiment, the liquid and gas streams are confined within lengths smaller than the observed longitudinal wavelength. The fact that confinement can trigger absolute instability in shear flows has been evidenced in recent years by Healey (2007, 2009), Juniper (2008) and Rees & Juniper (2010). The absolute instability observed by Fuster *et al.* (2013) and Otto *et al.* (2013) is of a different type, occurring between the shear instability branch and a branch located below, and is controlled by surface tension. We investigate in the following how including in the spatiotemporal analysis a confinement similar to the experimental one affects predictions.

2. Method

We consider Navier–Stokes equations for a base flow $\boldsymbol{U} = (U(y), 0, 0)$ and a small perturbation $\boldsymbol{u}(x, y, t)$ (coordinate system shown in figure 1). After linearization of this two-dimensional problem, we look for normal mode solutions of the form $\tilde{\boldsymbol{u}}(k, y, \omega)\mathrm{e}^{\mathrm{i}(kx-\omega t)}$ and obtain the classical Orr–Sommerfeld equation for the cross-stream velocity component of the perturbation in Fourier space $\tilde{v}(k, y, \omega)$ in each fluid (Otto *et al.* 2013). Boundary conditions are a solid wall at $y = -H_L$, and another solid wall at a distance $y = L_G$ on the gas side. For the present study, we take L_G to be 10 times larger than other scales in the problem, typically $L_G = 30\max(H_G, H_L)$, to ensure that no confinement occurs due to this wall. The method we use for solving this problem is different from the method used by Fuster *et al.* (2013) or Otto *et al.* (2013): instead of using a spectral method, we solve for the velocity perturbation $\tilde{v}(k, y, \omega)$ in real space, with a Runge–Kutta method. In each phase, integration is carried out from the solid wall, where both velocity components must be zero, to the interface, where continuity of tangential and normal velocities, as well as continuity of tangential and normal stresses, is enforced. Surface tension and gravity normal to the interface, which may affect prediction for large wavelength, are included in the normal stress equation. In order to ensure that both solutions satisfying $\tilde{v} = 0$ and $\partial\tilde{v}/\partial y = 0$ at the solid walls remain independent during integration, we orthonormalize the associated four-dimensional vectors at each time step within the Runge–Kutta algorithm with the procedure described in Asmolov (1999) and Matas,

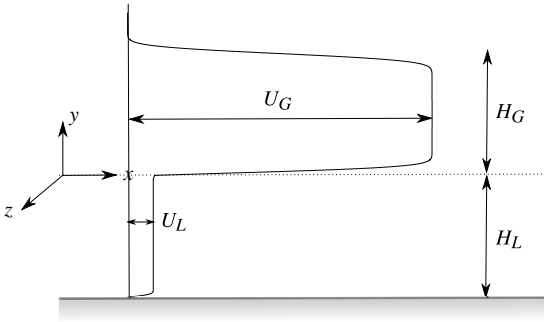

FIGURE 1. Sketch showing the typical base flow profile, including finite liquid and gas stream thicknesses.

Morris & Guazzelli (2009). The dispersion relation is then solved with a shooting method (two-dimensional Newton–Raphson method). Contrary to the spectral method, the present shooting method does not provide us with the whole set of eigenmodes: however, it is well adapted to the present aim, which is to focus on a given set of parameters close to experimental conditions.

We chose the same family of base flow profiles used by Otto *et al.* (2013), namely a sum of error functions accounting for the wake due to the splitter plate between the liquid and gas streams. Additional error function cutoff terms are added to account for the finite H_G and H_L that we wish to include in the present study:

$$U(y) = \begin{cases} \left\{ U_G \operatorname{erf}\left(\dfrac{y}{\delta_G}\right) + U_i \left[1 - \operatorname{erf}\left(\dfrac{y}{\delta_d \delta_L}\right)\right]\right\} \\ \quad \times \dfrac{1}{2}\left[1 + \operatorname{erf}\left(\dfrac{H_G - y}{\delta_G}\right)\right] \quad \text{for } 0 < y < L_G, \\ -\left\{ U_L \operatorname{erf}\left(\dfrac{y}{\delta_L}\right) + U_i \left[1 + \operatorname{erf}\left(\dfrac{y}{\delta_d \delta_L}\right)\right]\right\} \\ \quad \times \operatorname{erf}\left(\dfrac{y + H_L}{\delta_L}\right) \quad \text{for } -H_L < y < 0, \end{cases} \tag{2.1}$$

where U_i is the interface velocity $U_i = (U_G \mu_G/\delta_G + U_L \mu_L/\delta_L)/(\mu_G + \mu_L)\delta_d \delta_L$, with μ_G and μ_L the dynamical viscosities of gas and liquid, and δ_L the liquid boundary layer. The dimensionless parameter δ_d allows control of the amplitude of the velocity deficit: for $\delta_d = 1$ there is no velocity deficit (as in figure 1), while for $\delta_d \ll 1$ the interface velocity goes down to zero (Otto *et al.* 2013).

In order to facilitate comparison with experiments, we set the gas vorticity thickness to the value measured in experiments. The experimental δ_G is well approximated (see Raynal 1997; Matas *et al.* 2011) by $\delta_G = 6H_G/\sqrt{U_G H_G \rho_G/\mu_G}$. The liquid boundary layer is set to a constant value of $\delta_L = 500$ μm, close to the value measured in the experiment for the relevant range of liquid velocities (particle image velocimetry measurement). Note finally that the above expression is a fit of the mean velocity profile: though experimental air and water flows are turbulent for the Reynolds numbers of interest, fluctuations are not included in the present analysis.

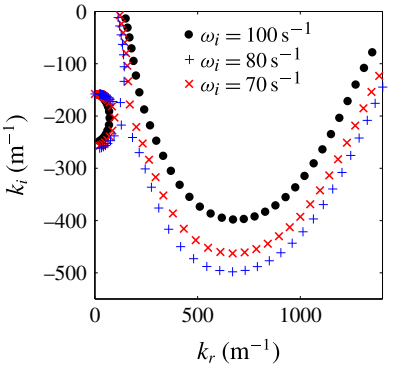

FIGURE 2. (Colour online) Pinching at positive ω_{0i} occurs between confinement and shear controlled branches when confinement is taken into account; $U_G = 27$ m s^{-1}, $U_L = 0.26$ m s^{-1}, $\delta_d = 1$, $H_G = 1$ cm and $H_L = 1$ cm. Symbols correspond to ω_r in the range (80–680) s^{-1}.

3. Results and discussion

We now confront the predictions obtained with this method to the air–water experimental data of Matas *et al.* (2011). We first consider their series of data obtained at a fixed $U_G = 27$ m s^{-1}: the prediction of the viscous spatiotemporal analysis without confinement for this series overestimates the experimental data by a factor of 2 for most liquid velocities (see figure 31*d* of Otto *et al.* 2013). Figure 2 shows what happens for $U_L = 0.26$ m s^{-1} when a confinement similar to the experimental one is taken into account and when ω_i, the imaginary part of ω, is reduced: a confinement branch appears along the k_i axis, and pinching between this branch and the shear instability branch occurs for positive ω_{0i}. While the shear instability branch involved in the pinching observed by Otto *et al.* (2013) at large U_L is what they call the weaker mode (as in figure 25*b* of their paper), the branch involved in the pinching mechanism of figure 2 is the stronger mode, which extends to lower wavenumbers. The confinement branch involved in the pinching is of the type described in Healey (2007): it arises because of the oscillatory nature of the confined perturbation when k is close to the imaginary axis. The frequency predicted without taking confinement into account would be the frequency corresponding to the minimum of the negative growth rate (there is no pinch point on the weaker mode for the conditions of figure 2), namely 66 Hz, while the pinching caused by confinement occurs for a much lower frequency of 28 Hz. The latter frequency is much closer to the experimental frequency $f_{exp} = 28.8$ Hz.

For the case of an absolute instability, nonlinearity is expected to affect the properties of the eigenmode at the pinch point, and comparison between growth rate at the pinch point and experimental spatial growth rate is therefore not attempted. It is however interesting to note the value of the wavenumber at the pinch point: figure 2 shows that the pinching induces a major reduction in the predicted wavenumber, from $k_r \approx 720$ m^{-1} down to $k_r \approx 140$ m^{-1}. The corresponding phase velocity ω_r/k_r (we denote ω_r the real part of ω) is then about 1.28 m s^{-1}, very close to the value given by (1.2), $U_c = 1.2$ m s^{-1}. Wave velocity was not measured in the experiment of Matas *et al.* (2011), but previous experiments by Raynal (1997) and Ben Rayana (2007) had both found wave velocity in close agreement with U_c. In addition, expression (1.2) for velocity U_c was derived by Dimotakis (1986) through a balance of dynamic

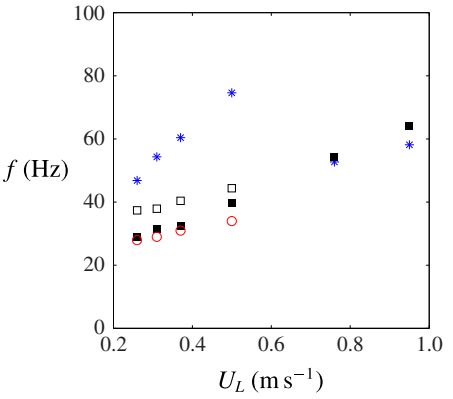

FIGURE 3. (Colour online) Comparison at $U_G = 27$ m s^{-1} between experimental data of Matas *et al.* (2011) (■) and available spatiotemporal predictions: ∗, prediction by Otto *et al.* (2013), for $\delta_d = 0.1$; ○, prediction taking into account confinement without any velocity deficit ($\delta_d = 1$); □, prediction with confinement and a velocity deficit ($\delta_d = 0.5$).

pressure, and a similar expression was found by Matas *et al.* (2011) in the frame of the inviscid linear theory via an asymptotic expansion in the limit of low density ratio. This expression therefore corresponds to a perturbation driven by an inviscid mechanism: the fact that the predicted phase velocity is close to (1.2) is a first indication that the dominant mechanism for these ω and k is inviscid. Note that the velocity associated with the most unstable modes in Fuster *et al.* (2013) or Otto *et al.* (2013), which are viscous modes, is closer to U_i and significantly lower than this estimate.

Figure 3 next shows how the predicted frequency compares to the experimental one (filled squares) for the experimental data at $U_G = 27$ m s^{-1} for each of the six liquid velocities investigated. The asterisks show the prediction of Otto *et al.* (2013) for $\delta_d = 0.1$, a prediction that works well for the two higher velocities, but clearly fails for the four lower velocities. For $\delta_d = 1$ the predictions of Otto *et al.* (2013) for all U_L far exceed experimental data (see figure 31*d* of their paper), and are not shown here. The circles show the frequency obtained at pinching when confinement is taken into account, for $\delta_d = 1$ (no velocity deficit): this frequency is in relatively good agreement with experimental data. Note that for the four lower liquid velocities the mode predicted by Otto *et al.* (2013) when $\delta_d = 1$ is associated with a convective mode, and the present absolute instability caused by confinement is therefore expected to dominate. For $\delta_d = 1$ and the two largest liquid velocities in this series, however, the pinching occurs at negative ω_{0i}, and the confinement mechanism is consequently not relevant.

If a velocity deficit is included in the base flow profile, the absolute instability is enhanced (i.e. it occurs at even larger ω_{0i}), and the frequency slightly increases too; these data are shown by the open squares in figure 3, for $\delta_d = 0.5$. If a stronger deficit is included ($\delta_d < 0.4$), the shear instability branch is displaced and the pinch point due to confinement disappears. Figure 4 shows the same comparison for the series of experimental data of Matas *et al.* (2011) at $U_G = 22$ m s^{-1}, and the same agreement is found when confinement is included. Figure 5 shows the variation of the absolute growth rate ω_{0i} at the pinch point: it decreases when U_L is increased, and eventually

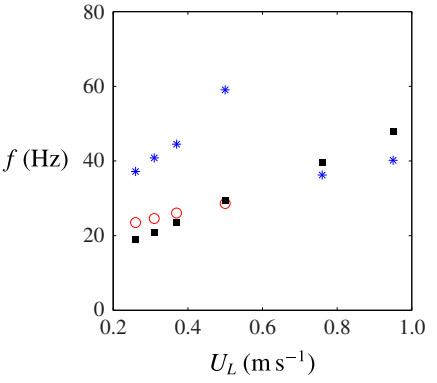

FIGURE 4. (Colour online) Comparison at $U_G = 22$ m s^{-1} between experimental data of Matas *et al.* (2011) (■) and available spatiotemporal predictions: ∗, prediction by Otto *et al.* (2013), for $\delta_d = 0.1$; ○, prediction taking into account confinement without any velocity deficit ($\delta_d = 1$).

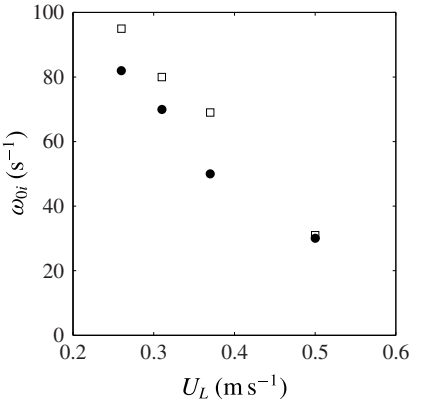

FIGURE 5. Variation of the absolute growth rate ω_{0i} at the pinch point caused by the confinement branch, as a function of liquid velocity, for fixed $U_G = 27$ m s^{-1}, $H_G = 1$ cm and $H_L = 1$ cm: ●, $\delta_d = 1$; □, $\delta_d = 0.5$. The growth rate decreases when liquid velocity is increased, and increases when a velocity deficit is included.

becomes negative for $U_L > 0.6$ m s^{-1}. The inclusion of a moderate velocity deficit ($\delta_d = 0.5$, open squares) leads to a slight increase of ω_{0i}.

The fact that agreement between prediction and experiments occurs for $\delta_d = 1$ at lower U_L, while it occurs for smaller δ_d at larger U_L, is consistent with the idea that the velocity deficit will be resorbed over a longer distance when the liquid velocity is larger. At any rate, only a global approach, in the sense introduced by Huerre & Monkewitz (1990), may clarify how mode selection occurs in the presence of strong spatial variations, when unstable modes predicted close to the splitter plate (where $\delta_d \ll 1$) differ from those farther downstream (where $\delta_d = 1$).

In order to clarify the nature of the dominant mechanism for the new pinch point caused by confinement, we carry out an energy budget similar to the one introduced by Boomkamp & Miesen (1996) for temporal modes. The energy budget can be

U_L (m s^{-1})	δ_d	REY_L	REY_G	TAN	DIS_L	DIS_G
0.26	1	3	80	23	−0.1	−7.8
0.31	1	3.2	84.3	20	−0.1	−8.8
0.37	1	3	82	21	−0.1	−8.2
0.5	1	2.7	82	21	−0.1	−7.9
0.74	0.1	3.3	51	330	−7.7	−280
1	0.1	1.6	−24	740	−17	−600

TABLE 1. Energy budget for the data (○) and (∗) of figure 3. Values are as a percentage of the total (positive) kinetic energy rate.

written as

$$\frac{\mathrm{d}E_{kin}}{\mathrm{d}t} = REY_L + REY_G + TAN + NOR + DIS_L + DIS_G. \tag{3.1}$$

Here E_{kin} is the total kinetic energy of the eigenmode (gas + liquid); REY_L (respectively REY_G) is the transfer of energy from the base flow to the perturbation via Reynolds stresses in the liquid (respectively gas) stream; TAN is the work of tangential stresses; NOR is the contribution of normal stresses (surface tension and gravity in the present case); and DIS_L (respectively DIS_G) is the dissipation in the liquid phase (respectively gas phase). The analytical expressions for each of these terms are very similar to the expressions given in Otto *et al.* (2013), and are not repeated here. The only differences here are that the wavenumber is complex, and that the kinetic energy variation term must be generalized to include a contribution from the spatial growth:

$$\begin{aligned}\frac{\mathrm{d}E_{kin}}{\mathrm{d}t} = {} & \omega_i \int_{-H_L}^{0} \rho_L(u^2+v^2)\mathrm{d}y - k_i \int_{-H_L}^{0} \rho_L(u^2+v^2)U(y)\mathrm{d}y \\ & + \omega_i \int_{0}^{L_G} \rho_G(u^2+v^2)\mathrm{d}y - k_i \int_{0}^{L_G} \rho_G(u^2+v^2)U(y)\mathrm{d}y.\end{aligned} \tag{3.2}$$

We compute the energy budget for the six data points of figure 3 showing the best agreement with experimental results, more precisely the four data points obtained with confinement for lower U_L and $\delta_d = 1$ (no velocity deficit), and the two points obtained by Otto *et al.* (2013) for $U_L = 0.74$ and 1 m s^{-1} (with a velocity deficit, $\delta_d = 0.1$). The energy contributions are normalized by the total positive kinetic energy rate. We omit the contribution of NOR, which is negligible for most of the present points. Table 1 shows that, for the four conditions for which confinement triggers the absolute instability, the mechanism is inviscid, and that the perturbation draws its energy from the gas side. This is consistent with phase velocity being close to U_c (1.2). For the two data points at larger velocity, the mechanism is confirmed to be viscous, driven by the work of interfacial tangential stresses (Otto *et al.* 2013). Dissipation occurs almost exclusively in the gas phase.

The idea behind the generalized budget of (3.1) is to identify among the right-hand contributions which are dominant and which are negligible when at the pinch point. It might be tempting to carry out the energy budget in a more classical form, in order to avoid the generalization to spatiotemporal modes. However, for a purely temporal mode, the results would depend very much on how the {spatiotemporal → temporal} transposition is made. For a purely temporal mode at the same ω_r as the

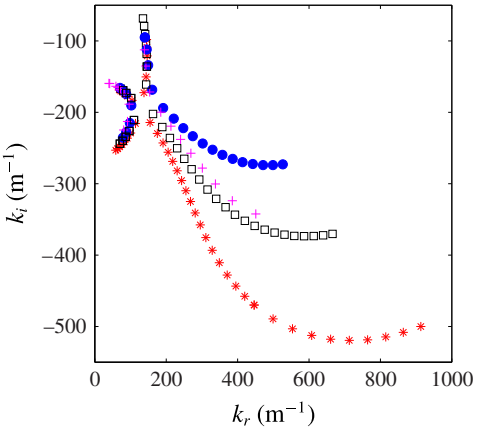

FIGURE 6. (Colour online) Impact of a variation in viscosity on spatial branches for $U_G = 27$ m s^{-1}, $U_L = 0.26$ m s^{-1} and $\delta_d = 1$: $*$, $\nu_G = 1.5 \times 10^{-5}$ m s^{-1}, $\nu_L = 10^{-6}$ m s^{-1} and $\omega_i = 85$ s^{-1}; □, $\nu_G = 1.5 \times 10^{-6}$ m s^{-1}, $\nu_L = 10^{-7}$ m s^{-1} and $\omega_i = 65$ s^{-1}; ●, $\nu_G = 1.5 \times 10^{-7}$ m s^{-1}, $\nu_L = 10^{-8}$ m s^{-1} and $\omega_i = 50$ s^{-1}; +, $\nu_G = 1.5 \times 10^{-7}$ m s^{-1}, $\nu_L = 10^{-6}$ m s^{-1} and $\omega_i = 45$ s^{-1}. The shear branch is displaced when viscosity is reduced, but the location of the pinch point associated with confinement remains unchanged.

pinch point, for example, and conditions of the first line of table 1, the wavenumber would become $k_r \approx 380$ m^{-1} instead of $k_r \approx 170$ m^{-1} for the spatiotemporal mode. For these conditions, the energy budget says the temporal mode is 85 % viscous (the same budget would be found for the spatiotemporal mode at this larger k_r). If a {spatiotemporal → spatial} comparison is carried out for the wavenumber of the pinch point, then the energy budget says the mode is 60 % viscous and 40 % viscous. Hence a transposition would be extremely sensitive to which ω and k values are retained.

At any rate, the inviscid nature of the instability for the pinch point due to confinement is confirmed by figure 6, which shows the impact of a reduction of viscosity on spatial branches for the case $U_G = 27$ m s^{-1} and $U_L = 0.26$ m s^{-1} (conditions of figure 2). When viscosity is reduced, the shear branch is impacted, but the confinement branch is unchanged, and the pinch point remains at the same location. Frequency at the pinch point slightly decreases when viscosity is reduced, from $f = 28$ Hz for $\nu_G = 1.5 \times 10^{-5}$ m s^{-1} and $\nu_L = 10^{-6}$ m s^{-1} down to $f = 20$ Hz for $\nu_G = 1.5 \times 10^{-7}$ m s^{-1} and $\nu_L = 10^{-8}$ m s^{-1}.

This result is satisfying, because it explains the paradox exposed in the introduction, namely why the simplified analysis proposed by Raynal (1997) was successful, and why the inclusion of viscosity in the analysis had degraded the quality of the prediction. The inclusion of viscosity gives rise to a much stronger shear mode based on the viscous mechanism (Boeck & Zaleski 2005; Otto *et al.* 2013), but resonance due to confinement triggers an absolute instability for the lower-wavenumber part of the shear branch, which is dominated by the inviscid mechanism. This occurs for all the lower liquid velocity points of Matas *et al.* (2011), as in figure 3. For the larger liquid velocity conditions, we find that the shear branch is displaced away from the confinement branch, and the mechanism is then the one predicted by Otto *et al.* (2013), an absolute instability between the shear branch controlled by viscosity and a lower branch controlled by surface tension.

The velocity profile considered in figure 1 includes both a finite H_G and a finite H_L. In order to clarify the influence of these thicknesses, we keep them equal and vary

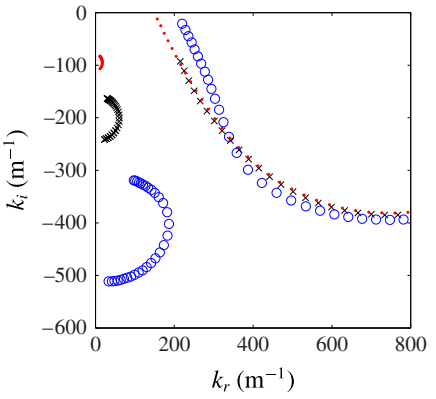

FIGURE 7. (Colour online) Change in the confinement branches when H_G and H_L are reduced, for fixed $U_G = 27$ m s^{-1}, $U_L = 0.26$ m s^{-1}, $\delta_d = 1$, $\omega_i = 120$ s^{-1} and ω_r in the range (60–430) s^{-1}: ●, $H_G = H_L = 2$ cm; ×, $H_G = H_L = 1$ cm; ○, $H_G = H_L = 0.5$ cm.

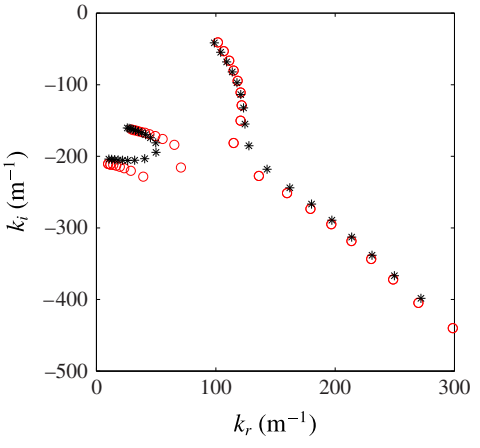

FIGURE 8. (Colour online) Pinching for $U_G = 27$ m s^{-1}, $U_L = 0.26$ m s^{-1}, $\delta_d = 1$, $\omega_i = 60$ s^{-1} and ω_r in the range (60–280) s^{-1}: ○, $H_G = 3$ cm and $H_L = 1$ cm; ∗, $H_G = 1$ cm and $H_L = 3$ cm. Both thicknesses play a symmetric role.

them, while keeping δ_G and δ_L constant and equal to their values for $H_G = H_L = H = 1$ cm. Figure 7 shows that the location of the confinement branch along the k_i axis behaves as $1/H$, and that the extension of the branches increases strongly with $1/H$: these branches therefore set the order of magnitude of k at the pinch point. If these thicknesses are distinct, we observe that their role is symmetric. Figure 8 shows two sets of branches obtained for ($H_G = 3$ cm; $H_L = 1$ cm) and for ($H_G = 1$ cm; $H_L = 3$ cm). Though experimentally a thick liquid and a thin gas stream may look quite different from a thin liquid stream and a thick gas stream, we find that the branches obtained in both situations are very close. They extend to the same *real*(k) as the branch obtained for $H_G = H_L = 1$ cm, the smaller length, the only difference being that the absolute growth rate ω_{0i} is significantly smaller for $H_G \neq H_L$ than for $H_G = H_L$. The fact that a symmetric confinement can enhance the absolute instability of a shear layer has already been pointed out in Healey (2009).

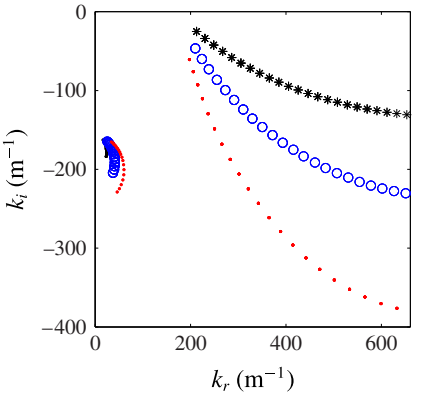

FIGURE 9. (Colour online) Influence of liquid velocity U_L, for fixed $U_G = 27$ m s^{-1}, $H_G = H_L = 1$ cm, $\delta_d = 1$ and $\omega_i = 120$ s^{-1}: ●, $U_L = 0.26$ m s^{-1}; ○, $U_L = 0.5$ m s^{-1}; ∗, $U_L = 1$ m s^{-1}. The ranges of ω_r are respectively (120–370), (170–500) and (260–820) s^{-1}. When liquid velocity is increased, the shear branch is shifted away from the confinement branch.

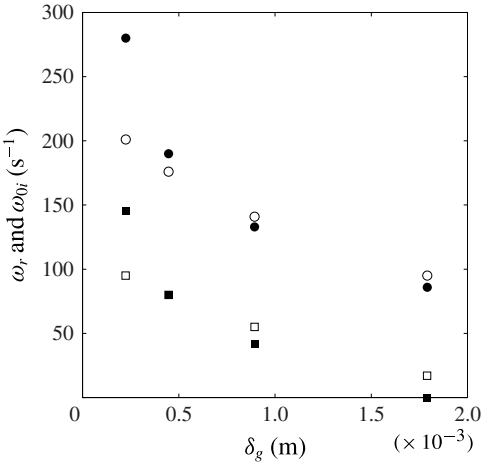

FIGURE 10. Influence of vorticity thickness δ_G on ω_r (circles) and ω_{0i} (squares), for fixed $U_G = 27$ m s^{-1}, $U_G = 0.26$ m s^{-1}, $\delta_d = 1$ and $H_G = H_L = 1$ cm. Open symbols correspond to $\delta_L = 500$ μm and filled symbols to $\delta_L = \delta_G$.

As shown in figure 3, the present mechanism dominates for the largest U_G/U_L cases but is absent for the largest liquid velocities investigated. Figure 9 sheds light on this behaviour. When U_L is increased, the maximum growth rate of the shear branch decreases. If the maximum growth rate of this branch, which is controlled by the viscous mechanism (Otto *et al.* 2013), is shifted above the location of the confinement branch, then the two branches cannot collide any more when ω_i is reduced.

All the above results have been obtained with δ_G set to its value in experiments, and with a fixed δ_L. We show in figure 10 the impact of δ_G for fixed U_G on both the real and imaginary parts of ω. Increasing δ_G causes a strong reduction in the frequency and absolute growth rate, both for $\delta_L = \delta_G$ (filled symbols) and for fixed $\delta_L = 500$ μm

(open symbols). The impact of δ_G on the wavenumber at the pinch point is weaker: k remains mostly constant when δ_G is increased, except for a slight decrease, and the location of the pinch point remains essentially controlled by the confinement branch.

The scalings of (1.1)–(1.3), in agreement with experiments, can be derived from the partially successful inviscid analysis. Up to now they had no justification in the context of viscous analyses. The fact that the energy of the perturbation is fed by the gas Reynolds stress indicates that the argument behind the simplified derivation of (1.1) is still valid. This is a significant result, since with $\omega \sim U_G/\delta_G$ we recover the $f \sim U_G^{3/2}$ scaling observed in most experimental studies, where δ_G scales as $U_G^{-1/2}$. The instability predicted here is absolute, and in the experiment nonlinearity is therefore expected to take over: the same arguments used by Dimotakis (1986) to derive (1.2) are expected to hold. Provided this is valid for the waves generated by the present mechanism, the scaling law (1.3) for the wavelength can then be derived from the scalings for velocity and frequency.

Acknowledgements

This project has been supported by the FIRST (Fuel Injector Research for Sustainable Transport) project supported by the European Commission under the Seventh Framework Programme. The LEGI laboratory is part of the LabEx Tec 21 (Investissements d'Avenir – grant agreement no. ANR-11-LABX-0030).

REFERENCES

ASMOLOV, E. 1999 The inertial lift on a spherical particle in a plane Poiseuille flow at large channel Reynolds number. *J. Fluid Mech.* **381**, 63–87.

BEN RAYANA, F. 2007 Contribution à l'étude des instabilités interfaciales liquide–gaz en atomisation assistée et tailles de gouttes. PhD thesis, INP Grenoble, France.

BOECK, T. & ZALESKI, S. 2005 Viscous versus inviscid instability of two-phase mixing layers with continuous velocity profile. *Phys. Fluids* **17**, 032106.

BOOMKAMP, P. & MIESEN, R. 1996 Classification of instabilities in parallel two-phase flow. *Intl J. Multiphase Flow* **22**, 67–88.

CHARRU, F. & HINCH, E. J. 2000 'Phase diagram' of interfacial instabilities in a two-layer Couette flow and mechanism of the long-wave instability. *J. Fluid Mech.* **414**, 195–223.

DIMOTAKIS, P. E. 1986 Two-dimensional shear-layer entrainment. *AIAA J.* **24**, 1791–1796.

EGGERS, J. & VILLERMAUX, E. 2008 Physics of liquid jets. *Rep. Prog. Phys.* **71**, 036601.

FUSTER, D., MATAS, J.-P., MARTY, S., POPINET, S., HOEPFFNER, J., CARTELLIER, A. & ZALESKI, S. 2013 Instability regimes in the primary breakup region of planar coflowing sheets. *J. Fluid Mech.* **736**, 150–176.

HEALEY, J. J. 2007 Enhancing the absolute instability of a boundary layer by adding a far-away plate. *J. Fluid Mech.* **579**, 29–61.

HEALEY, J. J. 2009 Destabilizing effects of confinement on homogeneous mixing layers. *J. Fluid Mech.* **623**, 241.

HINCH, E. J. 1984 A note on the mechanism of the instability at the interface between two fluids. *J. Fluid Mech.* **144**, 463–465.

HOOPER, A. P. & BOYD, W. G. C. 1983 Shear-flow instability at the interface between two viscous fluids. *J. Fluid Mech.* **128**, 507–528.

HOOPER, A. P. & BOYD, W. G. C. 1987 Shear-flow instability due to a wall and a viscosity discontinuity at the interface. *J. Fluid Mech.* **179**, 201–225.

HUERRE, P. & MONKEWITZ, P. A. 1990 Local and global instabilities in spatially developing flows. *Annu. Rev. Fluid Mech.* **22**, 473–537.

JUNIPER, M. P. 2008 The effect of confinement on the stability of non-swirling round jet/wake flows. *J. Fluid Mech.* **605**, 227–252.

LEFEBVRE, A. 1989 *Atomization and Sprays*. Hemisphere.

MARMOTTANT, P. & VILLERMAUX, E. 2004 On spray formation. *J. Fluid Mech.* **498**, 73–111.

MATAS, J.-P., MARTY, S. & CARTELLIER, A. 2011 Experimental and analytical study of a gas–liquid mixing layer. *Phys. Fluids* **23**, 094112.

MATAS, J.-P., MORRIS, J. F. & GUAZZELLI, E. 2009 Lateral force on a rigid sphere in large-inertia laminar pipe flow. *J. Fluid Mech.* **621**, 59–67.

OTTO, T., ROSSI, M. & BOECK, T. 2013 Viscous instability of a sheared liquid–gas interface: dependence on fluid properties and basic velocity profile. *Phys. Fluids* **25**, 032103.

RAYLEIGH, LORD 1879 On the stability, or instability, of certain fluid motions. *Proc. Lond. Math. Soc.* **11**, 57–72.

RAYNAL, L. 1997 Instabilité et entraînement à l'interface d'une couche de mélange liquide–gaz. PhD thesis, Université Joseph Fourier Grenoble I, France.

RAYNAL, L., VILLERMAUX, E., LASHERAS, J. & HOPFINGER, E. J. 1997 Primary instability in liquid gas shear layers. In *11th Symposium on Turbulent Shear Flows, 7–10 September 1997, Grenoble, France, Vol. 3*, pp. 27.1–27.5, OCLC 40626641, INP-CNRS-UJF.

REES, S. J. & JUNIPER, M. P. 2010 The effect of confinement on the stability of viscous planar jets and wakes. *J. Fluid Mech.* **656**, 309–336.

YIH, C. S. 1967 Instability due to viscous stratification. *J. Fluid Mech.* **27**, 337–352.